

Cite this article as: Cardinal Sandrine, Pelletier Jean-Marc, Kato Hidemi. Thermal Stability and Thermoplastic Formability of Pd<sub>20</sub>Pt<sub>20</sub>Cu<sub>20</sub>Ni<sub>20</sub>P<sub>20</sub> High Entropy Metallic Glass[J]. Rare Metal Materials and Engineering, 2024, 53(01): 1-7. DOI: 10.12442/j.issn.1002-185X.20230842.

ARTICLE

# Thermal Stability and Thermoplastic Formability of Pd<sub>20</sub>Pt<sub>20</sub>Cu<sub>20</sub>Ni<sub>20</sub>P<sub>20</sub> High Entropy Metallic Glass

Cardinal Sandrine<sup>1</sup>, Pelletier Jean-Marc<sup>1</sup>, Kato Hidemi<sup>2</sup>

<sup>1</sup>Institut National des Sciences Appliquées de Lyon, Université de Lyon, Lyon F-69621, France; <sup>2</sup>Institute for Metal Materials Research, Tohoku University, Sendai 980-8577, Japan

**Abstract:** Thermal stability and thermo-mechanical properties of Pd<sub>20</sub>Pt<sub>20</sub>Cu<sub>20</sub>Ni<sub>20</sub>P<sub>20</sub> high entropy metallic glass (HEMG) were investigated by differential scanning calorimetry, X-ray diffraction, and thermomechanical analysis. Results show that compared with other classical precious metal-based metallic glasses, Pd<sub>20</sub>Pt<sub>20</sub>Cu<sub>20</sub>Ni<sub>20</sub>P<sub>20</sub> HEMG presents comparable performance with distinct characteristics.

**Key words:** high entropy alloy; metallic glass; thermoplastic forming; crystallization

The order in solid materials is an old but relevant problem in metal material study. Many materials are crystalline of single-phase or multi-phase and thus exhibit long-range atomic order. Multi-phase materials include composites or alloys containing precipitates. Single-phase materials mainly involve the solid solutions, such as conventional steels or structurally hardened aluminum alloys. Rapid cooling from elevated temperature leads to the formation of solid solution, which is thermally unstable in most cases. Annealing leads to the formation of several phases and then multi-phases materials can be obtained.

Recently, high entropy alloys (HEAs) have been widely developed, based on the iron-based FeCrMnNiCo alloys<sup>[1]</sup>. Afterwards, many other elements, such as Zr and Ti, are added into HEAs for investigation<sup>[2]</sup>. HEAs normally contain at least five elements with equal or similar contents. For example, Cantor et al<sup>[1]</sup> prepared the typical Fe<sub>20</sub>Cr<sub>20</sub>Mn<sub>20</sub>Ni<sub>20</sub>Co<sub>20</sub> (at%) HEA. HEAs can also be composed of 6–8 components<sup>[3–7]</sup>. Regardless of the number of components, HEAs are usually characterized by high mixing entropy  $S_m$ . For a multi-component system, the mixing entropy can be defined, as follows:

$$S_m = -R \sum_{i=1}^N c_i \ln c_i \quad \text{with} \quad \sum_{i=1}^N c_i = 1 \quad (1)$$

where  $N$  is the total number of component elements,  $c$  is the element content,  $i$  is the order of element, and  $R$  is gas constant.

Generally, the  $S_m$  value of HEAs is greater than  $1.5R$ <sup>[1,6]</sup>. Attributed to their specific structures, HEA exhibits superior properties than the traditional alloys with conventional crystalline structures do by preventing the formation of intermetallic compounds. HEAs are principally composed of simple crystalline structures, such as face-centered cubic (fcc) and body-centered cubic (bcc) crystalline structures.

Great disorder can be found in metallic glasses (MGs), such as Au<sub>75</sub>Si<sub>25</sub> alloy<sup>[8]</sup>. Initially, the alloy formation requires extremely high quenching rates from liquid state, which restricts the manufactured part size. Thus, new components are developed and the critical quenching rate can be decreased to 1 K/s. Therefore, bulk MG with large size of several centimeters in diameter can be produced<sup>[9–22]</sup>. It is reported that the as-prepared bulk MG has the largest diameter of more than 8 cm<sup>[23]</sup>. Similar to polymer, MGs have glass transition characteristic. The absence of crystalline structure results in the superb mechanical properties and good resistance against wear and corrosion.

Due to the specific atomic disorder, some HEAs can even be elaborated at amorphous state to reach the dimension exceeding one centimeter<sup>[4–5,7–8,24–33]</sup>, namely high entropy metallic glasses (HEMGs). HEMGs are amorphous alloys with at least five elements of equiatomic (or nearly equiatomic) content, and they have excellent properties due to

Received date: December 24, 2023

Corresponding author: Pelletier Jean-Marc, Ph. D., Professor, Institut National des Sciences Appliquées de Lyon, Université de Lyon, Lyon F-69621, France, E-mail: jean-marc.pelletier@insa-lyon.fr

Copyright © 2024, Northwest Institute for Nonferrous Metal Research. Published by Science Press. All rights reserved.

their high entropy, showing great potential in applications. To develop such materials, shaping is an important process, particularly aiming to improve their thermal formability. A typical HEMG is  $\text{Pt}_{20}\text{Pd}_{20}\text{Cu}_{20}\text{Ni}_{20}\text{P}_{20}$  precious metal alloy<sup>[34–35]</sup>, which has excellent corrosion resistance and shows great potential in the medical field. Although other bulk MGs based on precious metals have also been investigated, including Au-, Pt-, and Pd-based alloys, they are not considered as HEAs<sup>[17,36–38]</sup>. Thus, HEMGs should be compared with classical bulk MGs of similar composition. Additionally, MG has supercooled liquid region, which is beneficial to obtain net shaped geometry instead of crystalline.

The viscosity ( $\eta$ ) is gradually decreased with increasing the temperature ( $T$ ) in the supercooled liquid region. When the temperature exceeds the glass transition temperature ( $T_g$ ), MG softens and can be deformed by small pressure. This softening phenomenon is critical for thermoplastic forming of MGs. The decrease in viscosity can be characterized by the fragility parameter ( $m$ ), as follows:

$$m = -\frac{\partial \lg \eta}{\partial \left(\frac{T_g}{T}\right)} \Big|_{T=T_g} \quad (2)$$

Good thermal formability requires low viscosity, i. e., high fragility. Silica has low fragility value of 25–28, MG has intermediate fragility, and organic compounds have high fragility value (the highest fragility value is 137), indicating that MG is at the favorable state. However, because bulk MGs are at the non-equilibrium state, they cannot always be thermally stable. Thus, crystallization can be observed at high temperatures, which results in a rapid increase in the viscosity and weakens the thermal formability. Kato et al<sup>[38]</sup> studied the correlation between fragility and thermal stability with deformability of Pt- and Pd-based MGs and the optimal workability with high fragility and high thermal stability.

It is necessary to operate between the glass transition temperature ( $T_g$ ) and the onset crystallization temperature ( $T_x$ ). The greater the temperature difference between  $T_g$  and  $T_x$ , the better the thermal formability<sup>[12–14,21,36–52]</sup>. Due to its good glass forming ability and large supercooled liquid region (60 K), the  $\text{Pt}_{20}\text{Pd}_{20}\text{Cu}_{20}\text{Ni}_{20}\text{P}_{20}$  HEMG was selected for investigation<sup>[34]</sup>. In this research, the thermal stability and the evolution of viscosity with temperature of  $\text{Pt}_{20}\text{Pd}_{20}\text{Cu}_{20}\text{Ni}_{20}\text{P}_{20}$  HEMG were studied.

## 1 Experiment

The  $\text{Pd}_{20}\text{Pt}_{20}\text{Ni}_{20}\text{Cu}_{20}\text{P}_{20}$  (at%) master alloy was prepared by  $\text{B}_2\text{O}_3$  flux method (Tohoku University, Japan)<sup>[34,38]</sup>. The pure Pd, Pt, Ni, Cu, and P elements were mixed in the sealed and evacuated quartz tube under argon atmosphere, and then they were placed in the resistance heating furnace. For comparison, two classical Pt- and Pd-based HEMGs were also prepared and studied. The  $\text{Pd}_{43}\text{Ni}_{27}\text{Cu}_{10}\text{P}_{20}$  (at%) alloy was supplied by Vulkam Company (France). The  $\text{Pt}_{57.3}\text{Cu}_{14.6}\text{Ni}_{5.3}\text{P}_{22.3}$  (at%) alloy was prepared by Tohoku University using the HEA preparation method. Then, the rods with 5 mm in diameter and 40 mm in length were obtained.

The specimens were characterized<sup>[16,44]</sup> by X-ray diffractometer (XRD, Bruker D8 Advance diffractometer system, Cu-K $\alpha$  radiation with  $\lambda=0.1540$  nm), and their densities were measured by Archimede method. The crystallization kinetics were studied by high temperature X-ray diffractometer (HTXRD). The in-situ experiments were performed by Anton Paar HTK 1200 oven chamber under vacuum condition. The thermal stability was examined by differential scanning calorimetry (DSC) at heating rate of 10 and 20 K/min using standard commercial instrument (Pekin Elmer, DSC-7) under high purity dry nitrogen with flow rate of 20 mL/min.

Young's modulus ( $E$ ) and Poisson ratio ( $\nu$ ) were determined by ultrasonic measurements through wave runner. A pulser/receiver and two transducers (3.175 mm, 5 MHz) were used for pulse echo and velocity measurement in longitudinal and shear modes. Thermomechanical analysis (TMA) experiments were performed by classical dilatometer (Setaram TMA 92) with pure argon gas to avoid the oxidation of specimens. An alumina cylindrical end compression probe was used (diameter of 8 mm). A constant load of 1.5 N was applied on the cylindrical specimens with 3 mm in length and 5 mm in diameter. Therefore, the initial stress was about 76 kPa. Isothermal treatment or continuous heating treatment was performed. The continuous heating rates were 1, 5, and 10 K/min. The absolute error of deformation is about 10  $\mu\text{m}$ . The penetration depth ( $\Delta L$ ) was recorded as a function of temperature or time during isothermal annealing. TMA cannot only be employed to examine the thermal expansion, but also be used to deduce viscosity<sup>[38,44]</sup>. Vickers hardness ( $\text{HV}_{0.05}$ ) measurements were performed on mirror-polished specimens through Testwell durometer.

## 2 Results and Discussion

### 2.1 Physical properties

Fig. 1a presents XRD pattern of the  $\text{Pd}_{20}\text{Pt}_{20}\text{Ni}_{20}\text{Cu}_{20}\text{P}_{20}$  HEMG. Broad diffraction peak without any crystalline peak indicates that the as-cast  $\text{Pd}_{20}\text{Pt}_{20}\text{Ni}_{20}\text{Cu}_{20}\text{P}_{20}$  HEMG is amorphous.

Fig. 1b shows DSC curve of  $\text{Pt}_{20}\text{Pd}_{20}\text{Cu}_{20}\text{Ni}_{20}\text{P}_{20}$  HEMG during heating process at heating rate of 10 K/min. It can be seen that the glass transition temperature  $T_g=296$  °C and the onset crystallization temperature  $T_x=367$  °C. The thermal properties of classical  $\text{Pd}_{43}\text{Ni}_{27}\text{Cu}_{10}\text{P}_{20}$  and  $\text{Pt}_{57.3}\text{Cu}_{14.6}\text{Ni}_{5.3}\text{P}_{22.3}$  MGs were characterized under the same conditions. The values of  $T_g$ ,  $T_x$ , and  $\Delta T_{xg}=T_x-T_g$  at heating rates of 10 and 20 K/min are listed in Table 1.

Compared with the classical Pd- and Pt-based MGs, the  $\text{Pd}_{20}\text{Pt}_{20}\text{Ni}_{20}\text{Cu}_{20}\text{P}_{20}$  HEMG exhibits a large supercooled region  $\Delta T_{xg}=71$  °C, which is similar to that of the Pt-based MG but lower to that of Pd-based MG.  $T_x$  decreases from 393 °C to 367 °C, implying that although the stability of HEMG at the supercooled liquid state is not enhanced, the glass forming ability is still good, presenting potential for thermoplastic forming operations.

The crystallization phenomenon in  $\text{Pd}_{20}\text{Pt}_{20}\text{Ni}_{20}\text{Cu}_{20}\text{P}_{20}$

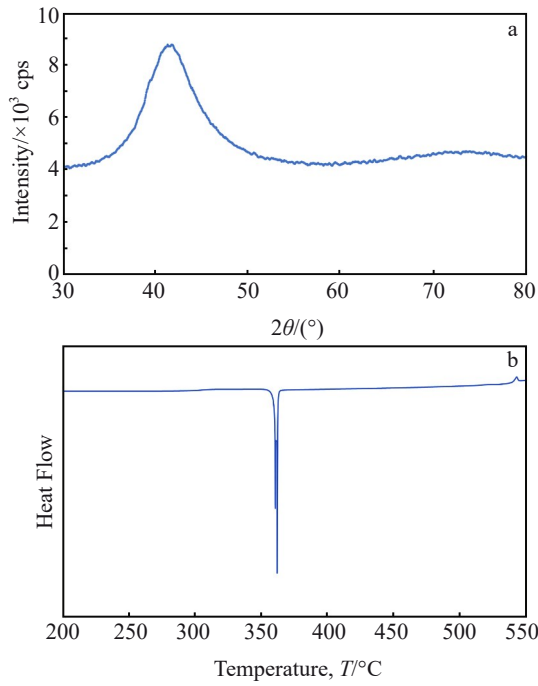


Fig.1 XRD pattern (a) and DSC curve (b) of Pd<sub>20</sub>Pt<sub>20</sub>Ni<sub>20</sub>Cu<sub>20</sub>P<sub>20</sub> HEMG

**Table 1 Characteristic temperatures of Pd<sub>20</sub>Pt<sub>20</sub>Ni<sub>20</sub>Cu<sub>20</sub>P<sub>20</sub> HEMG, Pd<sub>43</sub>Ni<sub>27</sub>Cu<sub>10</sub>P<sub>20</sub> MG, and Pt<sub>57.3</sub>Cu<sub>14.6</sub>Ni<sub>5.3</sub>P<sub>22.3</sub> MG**

Alloy	Heating rate/K·min <sup>-1</sup>	T <sub>g</sub> /°C	T <sub>x</sub> /°C	ΔT <sub>xg</sub> /°C
Pt <sub>20</sub> Pd <sub>20</sub> Cu <sub>20</sub> Ni <sub>20</sub> P <sub>20</sub>	10	293	360	67
	20	296	367	71
Pd <sub>43</sub> Ni <sub>27</sub> Cu <sub>10</sub> P <sub>20</sub>	10	296	383	87
	20	305	393	88
Pt <sub>57.3</sub> Cu <sub>14.6</sub> Ni <sub>5.3</sub> P <sub>22.3</sub>	10	226	295	69
	20	228	299	71

HEMG occurs within a very narrow temperature range, indicating that the crystallization occurs rapidly. Pt-based MG presents the similar results, whereas the crystallization of Pd-based MG occurs within a larger temperature range.

In order to further characterize the crystallization phenomenon, the in-situ XRD analyses were conducted at high temperatures. Continuous heating was performed to evaluate the effect of temperature and time on crystallization in the supercooled region. The specimen was firstly heated to 190 °C at heating rate of 20 K/min. Then, XRD patterns of HEMG specimen during heating from 190 °C to 400 °C are recorded with temperature interval of 5 °C. The average heating rate is about 0.8 K/min in this case. XRD pattern of HEMG specimen after isothermal annealing is also recorded for comparison.

Fig. 2a and 2b show in-situ XRD patterns of Pd<sub>20</sub>Pt<sub>20</sub>Ni<sub>20</sub>Cu<sub>20</sub>P<sub>20</sub> HEMG during continuous heating process and after isothermal annealing process at 400 °C, respectively. Only broad diffraction patterns can be observed at the glassy state

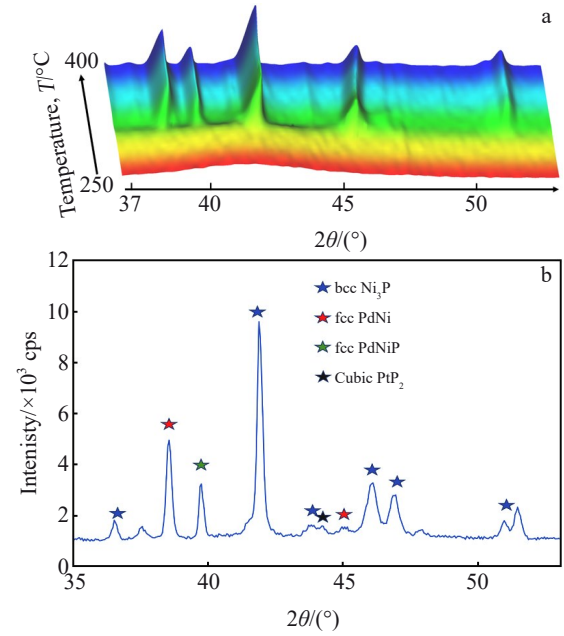


Fig.2 In-situ XRD patterns of Pd<sub>20</sub>Pt<sub>20</sub>Ni<sub>20</sub>Cu<sub>20</sub>P<sub>20</sub> HEMG during continuous heating process (a) and after isothermal annealing process at 400 °C (b)

and in the supercooled liquid region. At 315 °C, different crystalline phases appear simultaneously and grow until complete crystallization at 400 °C. According to XRD results, crystallization occurs earlier than the case according to DSC results (367 °C). This difference is caused by the difference in average heating rate. Considering the temperature interval, the average heating rate is about 0.8 °C/min during HTXRD test, whereas that in DSC measurement is constant of 10 °C/min. Pd<sub>20</sub>Pt<sub>20</sub>Ni<sub>20</sub>Cu<sub>20</sub>P<sub>20</sub> HEMG suffers crystallization and changes into multi-phases, which include body-centered tetragonal (bct) -Ni<sub>3</sub>P phase, a common phase in Pd-based bulk MG. Takeuchi et al.<sup>[53]</sup> found that in addition to bct- Ni<sub>3</sub>P phase, other simple crystalline phases also exist in Pd-based bulk MGs, such as fcc phase, cubic phase, Ni<sub>2</sub>Pd<sub>2</sub>P, (Ni, Pd), and PtP<sub>2</sub>, and the main phase is monoclinic. Similar results are also reported for Pt-based bulk MGs: their main crystalline phases are monoclinic P<sub>2</sub>Pt<sub>5</sub>, CuP<sub>2</sub>, and NiP<sub>2</sub><sup>[53-54]</sup>.

Therefore, it can be inferred that the thermal stability in supercooled region (between 295 and 310 °C) is a function of annealing time. Fig. 3a shows the in-situ XRD patterns of Pd<sub>20</sub>Pt<sub>20</sub>Ni<sub>20</sub>Cu<sub>20</sub>P<sub>20</sub> HEMG during isothermal annealing at 303 °C. The specimen is at amorphous state until approximately 40 min. Then, the crystallization occurs and lasts for several hours. The content of crystalline particles was measured and used to quantify the crystallization. Fig. 3b shows the crystalline particle contents during annealing at different temperatures. It can be seen that the crystalline particle content is increased with the annealing proceeding. Moreover, these curves can indicate the available time before crystallization, namely the available processing duration. Similar results can also be obtained for the Pd- and Pt-based

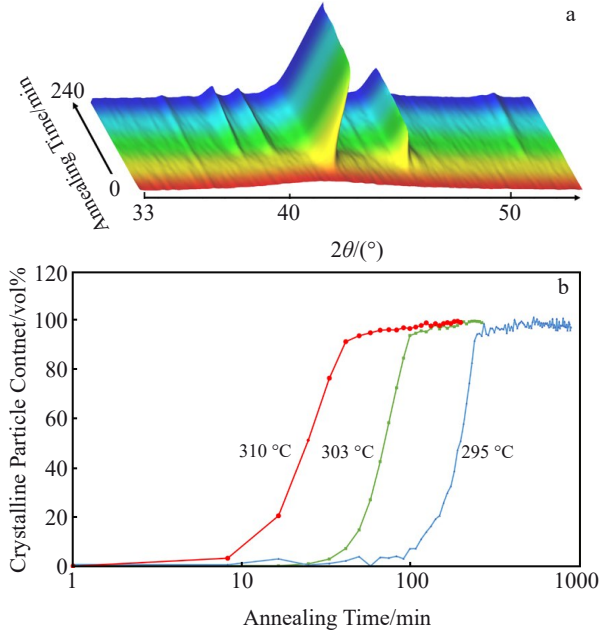


Fig.3 In-situ XRD patterns of Pd<sub>20</sub>Pt<sub>20</sub>Ni<sub>20</sub>Cu<sub>20</sub>P<sub>20</sub> HEMG during isothermal annealing at 303 °C (a); crystalline particle contents during annealing at different temperatures (b)

classical bulk MGs.

The incubation duration is about 10, 40, and 100 min at 310, 303, and 295 °C, respectively. According to these incubation durations under different isothermal temperatures, the corresponding time-temperature-transformation (TTT) diagram can be constructed. Fig. 4 shows TTT curves of Pd<sub>20</sub>Pt<sub>20</sub>Ni<sub>20</sub>Cu<sub>20</sub>P<sub>20</sub> HEMG, Pd-based MG, and Pt-based MG. The time-temperature window for thermal processing of HEMG can be obtained. It can be seen that Pd<sub>20</sub>Pt<sub>20</sub>Ni<sub>20</sub>Cu<sub>20</sub>P<sub>20</sub> HEMG has identical behavior as that of Pt-based MG, but the Pd-based MG shows longer incubation duration. Thus, the thermal stability of HEMG is not improved, compared with Pd-based MG. The evolution of crystalline particle content during isothermal annealing at different temperatures can be used to evaluate the apparent activation energy  $E_A$  for the crystallization process, as follows:

$$\ln t_{50}(T) = -E_A/kT + C \quad (3)$$

where  $t_{50}(T)$  is the duration to achieve 50% crystalline particles,  $C$  is a constant, and  $k$  is related parameter. The apparent activation energy  $E_A$  values of different alloys are shown in Table 2. It can be seen that these values are quite similar, and  $E_A$  value of Pd-based MG is slightly lower than that of HEMG and Pt-based MG.

## 2.2 TMA results

### 2.2.1 Continuous heating

TMA was conducted under load of 1.5 N at heating rates of 1, 5, and 10 K/min. Fig.5a shows the effect of temperature on deformation  $\Delta L/L$  of Pd<sub>20</sub>Pt<sub>20</sub>Ni<sub>20</sub>Cu<sub>20</sub>P<sub>20</sub> HEMG. The variation in length occurs in three different steps<sup>[44]</sup>: (1) at low temperatures, the variation is small, which is caused by the

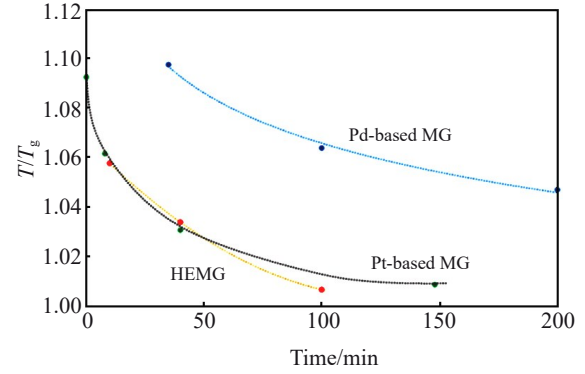


Fig.4 TTT curves of Pd<sub>20</sub>Pt<sub>20</sub>Ni<sub>20</sub>Cu<sub>20</sub>P<sub>20</sub> HEMG, Pd-based MG, and Pt-based MG

**Table 2** Apparent activation energy  $E_A$  required for crystallization of Pd<sub>20</sub>Pt<sub>20</sub>Ni<sub>20</sub>Cu<sub>20</sub>P<sub>20</sub> HEMG, Pd<sub>43</sub>Ni<sub>27</sub>Cu<sub>10</sub>P<sub>20</sub> MG, and Pt<sub>57.3</sub>Cu<sub>14.6</sub>Ni<sub>5.3</sub>P<sub>22.3</sub> MG (eV)

Alloy	Pd <sub>20</sub> Pt <sub>20</sub> Ni <sub>20</sub> Cu <sub>20</sub> P <sub>20</sub>	Pd <sub>43</sub> Ni <sub>27</sub> Cu <sub>10</sub> P <sub>20</sub>	Pt <sub>57.3</sub> Cu <sub>14.6</sub> Ni <sub>5.3</sub> P <sub>22.3</sub>
$E_A$	3.90	3.52	3.91

thermal expansion of the specimen; (2) at intermediate temperature (above the glass transition temperature), a large deformation occurs, which is attributed to the large decrease in viscosity; (3) at high temperature, the variation becomes less obvious, since the crystallization restricts the deformation.

The influence of heating rate is well demonstrated in Fig. 5a: the decrease in heating rate causes a shift of

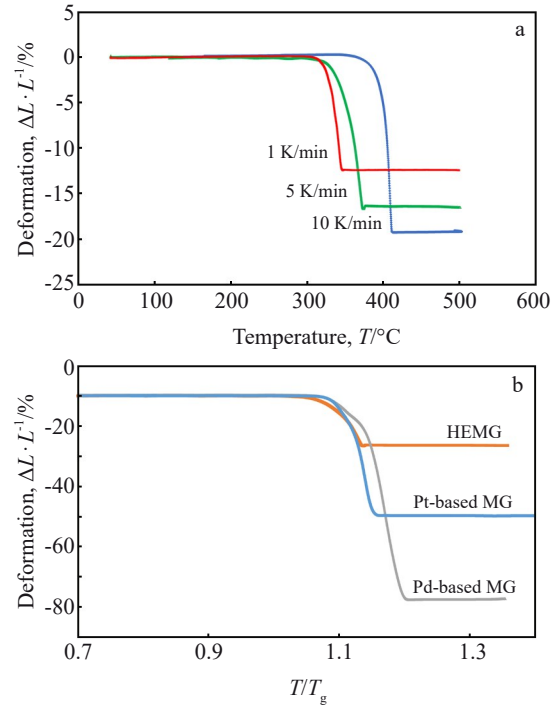


Fig.5 Deformation of Pd<sub>20</sub>Pt<sub>20</sub>Ni<sub>20</sub>Cu<sub>20</sub>P<sub>20</sub> HEMG during continuous heating at different heating rates (a); deformation of different alloys at heating rate of 5 K/min (b)

crystallization towards the lower temperature region and the deformation degradation of MG. The slower the heating rate, the longer the duration for atomic movement, and the lower the temperature for crystallization onset. Atomic movements in crystallization and deformation are both thermally activated phenomena. According to Fig. 5b, the temperature is normalized by  $T_g$  for better comparison. It can be seen that the  $\text{Pd}_{20}\text{Pt}_{20}\text{Ni}_{20}\text{Cu}_{20}\text{P}_{20}$  HEMG shows the smallest deformation degree.

### 2.2.2 Isothermal annealing

Fig. 6 shows the deformation of  $\text{Pd}_{20}\text{Pt}_{20}\text{Ni}_{20}\text{Cu}_{20}\text{P}_{20}$  HEMG during annealing at different temperatures with heating rate of 5 K/min. The increase in annealing temperature causes shorter deformation durations and more intense deformation. The higher the annealing temperature, the faster the diffusion. Therefore, crystallization occurs more rapidly. In addition, the higher the temperature, the lower the viscosity ( $\eta$ ).

### 2.2.3 Viscosity

The viscosity  $\eta$  is defined as the ratio of applied stress ( $\sigma$ ) to strain rate ( $\dot{\epsilon}$ ). Thus, the more intense deformation at higher temperature results from the decrease in viscosity. Viscosity can be deduced from the curves in Fig. 7<sup>[38,44]</sup>. Since a uniaxial load is applied,  $\eta = \sigma/3\dot{\epsilon}$ , neglecting the geometrical correction factor. According to the data in Fig. 7a, the viscosity

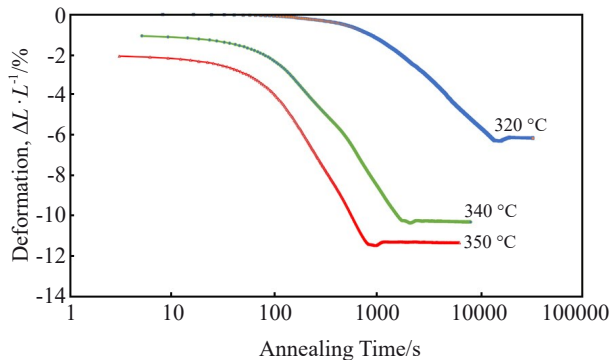


Fig. 6 Deformation of  $\text{Pd}_{20}\text{Pt}_{20}\text{Ni}_{20}\text{Cu}_{20}\text{P}_{20}$  HEMG during annealing at different temperatures with heating rate of 5 K/min

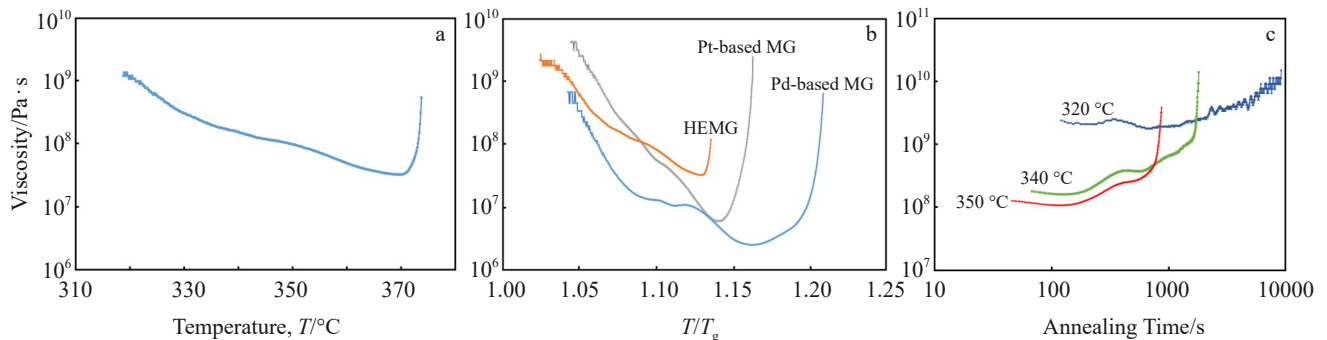


Fig. 7 Viscosity of  $\text{Pd}_{20}\text{Pt}_{20}\text{Ni}_{20}\text{Cu}_{20}\text{P}_{20}$  HEMG at different temperatures with heating rate of 5 K/min (a); viscosity of  $\text{Pd}_{20}\text{Pt}_{20}\text{Ni}_{20}\text{Cu}_{20}\text{P}_{20}$  HEMG, Pd-based MG, and Pt-based MG at different temperatures with heating rate of 5 K/min (b); viscosity of  $\text{Pd}_{20}\text{Pt}_{20}\text{Ni}_{20}\text{Cu}_{20}\text{P}_{20}$  HEMG during annealing at different temperatures (c)

can only be deduced in a limited range. Indeed, the viscosity can only be obtained when the thermal expansion effect is negligible compared with the thermal expansion, i. e., when the strain rate caused by the thermal expansion is lower than that caused by mechanical deformation. Thus, the viscosity at low temperature cannot be obtained, since the mechanical deformation is too small. At high temperatures, the crystalline particles also hinder the mechanical deformation.

In all amorphous materials, a rapid decrease in viscosity can be observed above the glass transition temperature. The minimum value is obtained before the onset of crystallization phenomenon as about  $3 \times 10^7$  Pa·s. Such low viscosity is attractive for the thermo-processing of metal materials. Although it is not as low as that of some polymers ( $10^3$ – $10^4$  Pa·s), but it is lower than that of many MGs, such as the classical zirconium-based alloys. As shown in Fig. 7b, the Pd-based MG exhibits lower viscosity, and the crystallization occurs later.

As shown in Fig. 7c, the viscosity is nearly constant and then it increases due to the formation of crystalline particles. The higher the annealing temperature, the lower the nearly constant value. Fig. 7c can be used to determine the optimal conditions for HEMG processing. It is found that  $\text{Pd}_{20}\text{Pt}_{20}\text{Ni}_{20}\text{Cu}_{20}\text{P}_{20}$  HEMG has fine characteristics, but it is not superior to the conventional alloys of similar composition.

## 2.3 Thermoforming

In order to illustrate the thermoforming of HEMG, a test was performed with specific mold (a lion head with size of 10 mm). A hot press device was used, and the processing temperature was 340 °C. Fig. 8 shows the appearance of HEMG specimen after thermoforming. It is found that the Vickers hardness of crystallized HEMG specimen is basically identical to that of the as-cast HEMG specimen ( $\text{HV}_{0.3} = 5194 \pm 98$  MPa), and no crystalline phase forms. Thus, the thermoforming does not modify the initial amorphous state.

## 2.4 Mechanical properties

The mechanical properties of  $\text{Pd}_{20}\text{Pt}_{20}\text{Ni}_{20}\text{Cu}_{20}\text{P}_{20}$  HEMG, Pd-based MG, and Pt-based MG are listed in Table 3. These results are in good agreement with those in



Fig.8 Appearance of HEMG specimen after thermoforming

Ref. [34 – 35, 55]. At the as-cast state, three alloys have basically the same Young's modulus, shear modulus, and Poisson ratio. The high Poisson ratio is beneficial to induce plastic deformation.

The Vickers hardness results of  $\text{Pd}_{20}\text{Pt}_{20}\text{Ni}_{20}\text{Cu}_{20}\text{P}_{20}$  HEMG, Pd-based MG, and Pt-based MG are listed in Table 4. The Vickers hardness values of three alloys at as-cast state are fairly similar. Crystallization causes a very large increase in Vickers hardness values for all alloys, and the most obvious increment is achieved for HEMG. The significantly high Vickers hardness is attributed to the presence of various intermetallic phases.

**Table 3 Mechanical properties of  $\text{Pd}_{20}\text{Pt}_{20}\text{Ni}_{20}\text{Cu}_{20}\text{P}_{20}$  HEMG,  $\text{Pd}_{43}\text{Ni}_{27}\text{Cu}_{10}\text{P}_{20}$  MG, and  $\text{Pt}_{57.3}\text{Cu}_{14.6}\text{Ni}_{5.3}\text{P}_{22.3}$  MG**

Alloy	Density, $\rho/\text{g}\cdot\text{cm}^{-3}$	Young's modulus, $E/\text{GPa}$	Poisson ratio, $\nu$	Shear modulus, $G/\text{GPa}$
$\text{Pd}_{20}\text{Pt}_{20}\text{Ni}_{20}\text{Cu}_{20}\text{P}_{20}$	11.3	98	0.410	34.7
$\text{Pd}_{43}\text{Ni}_{27}\text{Cu}_{10}\text{P}_{20}$	9.5	98	0.402	34.9
$\text{Pt}_{57.3}\text{Cu}_{14.6}\text{Ni}_{5.3}\text{P}_{22.3}$	14.9	94	0.420	32.6

**Table 4 Vickers hardness ( $\text{HV}_{0.3}$ ) of as-cast and crystallized  $\text{Pd}_{20}\text{Pt}_{20}\text{Ni}_{20}\text{Cu}_{20}\text{P}_{20}$  HEMG,  $\text{Pd}_{43}\text{Ni}_{27}\text{Cu}_{10}\text{P}_{20}$  MG, and  $\text{Pt}_{57.3}\text{Cu}_{14.6}\text{Ni}_{5.3}\text{P}_{22.3}$  MG ( $\times 9.8 \text{ MPa}$ )**

Alloy	$\text{Pd}_{20}\text{Pt}_{20}\text{Ni}_{20}\text{Cu}_{20}\text{P}_{20}$	$\text{Pd}_{43}\text{Ni}_{27}\text{Cu}_{10}\text{P}_{20}$	$\text{Pt}_{57.3}\text{Cu}_{14.6}\text{Ni}_{5.3}\text{P}_{22.3}$
As-cast	535 $\pm$ 8	435 $\pm$ 8	520 $\pm$ 5
Crystallized	845 $\pm$ 10	560 $\pm$ 10	633 $\pm$ 10

### 3 Conclusions

1)  $\text{Pd}_{20}\text{Pt}_{20}\text{Ni}_{20}\text{Cu}_{20}\text{P}_{20}$  high entropy metallic glass (HEMG),  $\text{Pd}_{43}\text{Ni}_{27}\text{Cu}_{10}\text{P}_{20}$  metallic glass (MG), and  $\text{Pt}_{57.3}\text{Cu}_{14.6}\text{Ni}_{5.3}\text{P}_{22.3}$  MG all have very high thermal stability with large supercooled liquid range.

2)  $\text{Pd}_{20}\text{Pt}_{20}\text{Ni}_{20}\text{Cu}_{20}\text{P}_{20}$  HEMG, Pd-based MG, and Pt-based MG can easily deform at high temperatures, which is beneficial to thermoforming shaping.

3) Although  $\text{Pd}_{20}\text{Pt}_{20}\text{Ni}_{20}\text{Cu}_{20}\text{P}_{20}$  HEMG has fine characteristics, it is not superior to the conventional alloys of similar composition.

### References

- Cantor B, Chang I T H, Knight P et al. *Materials Science and Engineering A*[J], 2004, 375: 213
- Li W D, Xie D, Li D Y et al. *Progress in Materials Science*[J], 2021, 118: 100777
- Li Y H, Wang S W, Wang X W et al. *Journal of Materials Science & Technology*[J], 2020, 43: 32
- Yang K, Fan X H, Li B et al. *Journal of Materials Research and Technology*[J], 2022, 17: 1911
- Du Y, Zhou Q, Wang H F. *Encyclopedia of Materials: Metals and Alloys*[M]. New York: Elsevier, 2022: 318
- Wada T, Jiang J, Yubuta K et al. *Materialia*[J], 2019, 7: 100372
- Ohashi Y, Wada T, Kato H. *Journal of Alloys and Compounds*[J], 2022, 915: 165366
- Klement W, Willens R H, Duwez P O L. *Nature*[J], 1960, 187(4740): 869
- Wang W H, Dong C, Shek C H. *Materials Science and Engineering R: Reports*[J], 2004, 44(2–3): 45
- Schroers J, Johnson W L. *Applied Physics Letters*[J], 2004, 84(18): 3666
- Takeuchi A, Inoue A. *Materials Transactions*[J], 2005, 46(12): 2817
- Ashby M F, Greer A L. *Scripta Materialia*[J], 2006, 54(3): 321
- Schuh C A, Hufnagel T C, Ramamurty U. *Acta Materialia*[J], 2007, 55(12): 4067
- Schroers J. *Advanced Materials*[J], 2010, 22(14): 1566
- Inoue A, Takeuchi A. *Acta Materialia*[J], 2011, 59(6): 2243
- Cardinal S, Pelletier J M, Eisenbart M et al. *Materials Science and Engineering A*[J], 2016, 660: 158
- Cardinal S, Qiao J, Pelletier J M et al. *Intermetallics*[J], 2015, 63: 73
- Qiao J E, Jia H L, Liaw P K. *Materials Science and Engineering R: Reports*[J], 2016, 100: 1
- Kruzic J J. *Advanced Engineering Materials*[J], 2016, 18(8): 1308
- Wang W H. *Progress in Materials Science*[J], 2019, 106: 100561
- Sohrabi N, Jhabvala J, Logé R E. *Metals*[J], 2021, 11(8): 1279
- Loye A M, Kwon H K, Dellal D et al. *Biomedical Materials*[J], 2021, 16(4): 45018
- Nishiyama N, Takenaka K, Miura H et al. *Intermetallics*[J],

- 2012, 30: 19
- 24 Jin J S, Li F W, Yin G et al. *Thermochimica Acta*[J], 2020, 690: 178650
- 25 Jalali A, Malekan M, Park E S et al. *Journal of Alloys and Compounds*[J], 2022, 892: 162220
- 26 Chen Y, Dai Z W, Jiang J Z. *Journal of Alloys and Compounds*[J], 2021, 866: 158852
- 27 Calin M, Vishnu J, Thirathipviwat P et al. *Materials Science and Engineering C*[J], 2021, 121: 111733
- 28 Li M C, Guan H M, Yang S et al. *Materials Science and Engineering A*[J], 2021, 805: 140542
- 29 Dehkordi Z K, Malekan M, Nili-Ahmadabadi M. *Journal of Non-crystalline Solids*[J], 2022, 576: 121265
- 30 Chen Q X, Li D M, Wu Y et al. *Materials Science and Engineering A*[J], 2022, 831: 142342
- 31 Shan F L, Sun T T, Song W D et al. *Journal of Non-crystalline Solids*[J], 2022, 587: 121608
- 32 Wang H, Chen J G, Luo H L et al. *Intermetallics*[J], 2022, 141: 107430
- 33 Huo J T, Li K Y, Zang B W et al. *Chinese Physics Letters*[J], 2022, 39(4): 46401
- 34 Takeuchi A, Chen N, Wada T et al. *Intermetallics*[J], 2011, 19(10): 1546
- 35 Duan Y J, Zhang L T, Wada T et al. *Journal of Materials Science & Technology*[J], 2022, 107: 82
- 36 Saotome Y, Itoh K, Zhang T et al. *Scripta Materialia*[J], 2001, 44(8-9): 1541
- 37 Schroers J. *JOM*[J], 2005, 57: 35
- 38 Kato H, Wada T, Hasegawa M et al. *Scripta Materialia*[J], 2006, 54(12): 2023
- 39 Kumar G, Tang H X, Schroers J. *Nature*[J], 2009, 457(7231): 868
- 40 Mauro J C, Yue Y, Ellison A J et al. *Proceedings of the National Academy of Sciences*[J], 2009, 106(47): 19780
- 41 Henann D L, Anand L. *Journal of the Mechanics and Physics of Solids*[J], 2010, 58(11): 1947
- 42 Sarac B, Kumar G, Hodges T et al. *Journal of Microelectromechanical Systems*[J], 2010, 20(1): 28
- 43 Chen N, Yang H A, Caron A et al. *Journal of Materials Science*[J], 2011, 46: 2091
- 44 Qiao J C, Cardinal S, Pelletier J M et al. *Journal of Alloys and Compounds*[J], 2015, 628: 357
- 45 Kato H, Wada T, Hasegawa M et al. *Scripta Materialia*[J], 2006, 54(12): 2023
- 46 Li N, Chen W, Liu L. *JOM*[J], 2016, 68: 1246
- 47 Monfared A, Liu W, Zhang L. *Journal of Alloys and Compounds*[J], 2017, 711: 235
- 48 Bera S, Sarac B, Balakin S et al. *Materials & Design*[J], 2017, 120: 204
- 49 Gross O, Riegler S S, Stolpe M et al. *Acta Materialia*[J], 2017, 141: 109
- 50 Bochtler B, Kruse O, Busch R. *Journal of Physics: Condensed Matter*[J], 2020, 32(24): 244002
- 51 Al-Mukadam R, Götz I K, Stolpe M et al. *Acta Materialia*[J], 2021, 221: 117370
- 52 Neuber N, Gross O, Frey M et al. *Acta Materialia*[J], 2021, 220: 117300
- 53 Takeuchi A, Chen N, Wada T et al. *Intermetallics*[J], 2011, 19(10): 1546
- 54 Jiang J Z, Saksl K. *Materials Science and Engineering A*[J], 2004, 375: 733
- 55 Duan Y J, Zhang L T, Qiao J C et al. *Physical Review Letters*[J], 2022, 129(7): 175501

## Pd<sub>20</sub>Pt<sub>20</sub>Cu<sub>20</sub>Ni<sub>20</sub>P<sub>20</sub>高熵金属玻璃的热稳定性和热塑成形性

Cardinal Sandrine<sup>1</sup>, Pelletier Jean-Marc<sup>1</sup>, Kato Hidemi<sup>2</sup>

(1. 里昂大学 里昂国立应用科学学院, 法国 里昂 F-69621)

(2. 东北大学 金属材料研究所, 日本 仙台 980-8577)

**摘要:** 采用差示扫描量热法、X射线衍射和热力学分析研究了Pd<sub>20</sub>Pt<sub>20</sub>Cu<sub>20</sub>Ni<sub>20</sub>P<sub>20</sub>高熵金属玻璃 (HEMG) 的热稳定性和热力学性能。结果表明, 与其他经典贵金属基金属玻璃相比, Pd<sub>20</sub>Pt<sub>20</sub>Cu<sub>20</sub>Ni<sub>20</sub>P<sub>20</sub> HEMG具有相当的性能和鲜明的特点。

**关键词:** 高熵合金; 金属玻璃; 热塑性成形; 结晶

作者简介: Cardinal Sandrine, 女, 1965年生, 博士, 教授, 里昂大学里昂国立应用科学学院, 法国 里昂 F-69621, E-mail: sandrine.cardinal@insa-lyon.fr